



Triaxial Compression Testing at Constant and Reducing Confining Pressure for the Mechanical Characterization of a Specific Type of Sandstone

Jiu-chang Zhang^{1,2} · Zhi-nan Lin³ · Bo Dong² · Rong-xin Guo¹

Received: 29 March 2020 / Accepted: 28 December 2020 / Published online: 9 February 2021
© The Author(s), under exclusive licence to Springer-Verlag GmbH, AT part of Springer Nature 2021

Abstract

In this study, constant confining pressure (CCP) and reducing confining pressure (RCP) triaxial compression tests were conducted for mechanical characterization of a sandstone material. These triaxial experiments were carried out within a range of confining pressure from 0 to 50 MPa. The experimental results revealed that the sandstone exhibits a significant ductile-semibrittle stress degradation behaviour in the post-peak region. It was found that the plastic flows are mostly perpendicular to the initial, ultimate, fracture, and residual yield surfaces. This demonstrates that the associated flow rule can be adopted to describe the macroscopic plastic deformation of the sandstone. With increasing confining pressure, the brittleness decreases and causes a transformation of the failure mode from tension-splitting failure to mixed tension-shear failure, and then to shear failure. The sandstone exhibits the same deformation and strength behaviours along the CCP and RCP stress paths, however, deformation and failure were more brittle in the RCP tests than in the CCP tests. This experimental investigation can provide an important technical reference for geotechnical engineering projects involving sandstone.

Keywords Sandstone · Mechanical characterization · Triaxial compression · Elasto-plastic behaviour · Post-peak failure

List of Symbols

| | | | |
|---------------------------|---|---|---|
| σ_1 and σ_2 | Major and intermediate principal stress, respectively | q_r | Residual strength |
| σ_3 | Minor principal stress, confining pressure | ϵ_1 | Major principal strain, axial strain |
| q | Deviatoric stress, deviatoric shear stress | ϵ_3 | Minor principal strain, radial strain |
| p | Mean stress | ϵ_{ij} , ϵ_{ij}^e and ϵ_{ij}^p | Total, elastic and plastic strain tensors, respectively |
| q_{cc} | Crack closure stress | γ_s , γ_s^e and γ_s^p | Total, elastic and plastic shear strains, respectively |
| q_{ci} | Crack initiation stress | ϵ_v , ϵ_v^e and ϵ_v^p | Total, elastic and plastic volume strains, respectively |
| q_{cd} | Crack damage stress | c and φ | Cohesion and internal friction angle for Mohr–Coulomb criterion |
| q_p | Peak strength | σ_u | Uniaxial characteristic strength |
| q_f | Failure strength | E | Elastic modulus |
| | | ν | Poisson's ratio |
| | | m and s | Strength parameters for Hoek–Brown criterion |
| | | $d\epsilon^p$ | Magnitude of plastic strain-increment |
| | | ψ | Plastic flow angle |
| | | α | Tangent angle of the yield surface |
| | | ΔW_{A-B}^e | Elastic energy withdrawn from the rock specimen |
| | | ΔW_{A-B}^a | Additional energy |
| | | ΔW_{A-B}^r | Post-peak rupture energy |

✉ Rong-xin Guo
guorx@kmust.edu.cn

¹ Yunnan Provincial Key Laboratory of Civil Engineering Disaster Prevention, Faculty of Civil Engineering and Mechanics, Kunming University of Science and Technology, Jingming South Road, Kunming 650500, China

² Department of Civil Engineering, Yunnan Minzu University, Yuehua Street, Kunming 650504, China

³ College of Civil and Architectural Engineering, Guangxi University of Science and Technology, Liuzhou 545006, China

| | |
|---------|---------------------------------------|
| M | Post-peak modulus |
| B_r | Brittleness index |
| β | Dip angle of primary rupture fracture |

1 Introduction

Sandstone is usually encountered in underground construction in Southwest China. In this area, due to dramatic changes of elevations between high mountains and deep valleys, sandstone is often subjected to high and complex stress states (Jiang and Wang 2002). In these environments, underground openings have caused engineering problems relevant to sandstones, such as rockbursts (Jiang and Wang 2002), creep deformations (Xu et al. 2011), and TBM jamming (Shang et al. 2005). In other parts of the world, underground engineering case studies relevant to sandstone behaviour have also been reported (Jeng et al. 2002; Li et al. 2019; Oliveira and Diederichs 2017; Soleiman Dehkordi et al. 2013).

In a deep tunnel excavation, surrounding rocks are subjected to the unloading of lateral confinements and the loading of vertical stresses. The redistribution of geostresses causes damage and deterioration of the mechanical properties of the surrounding rocks. Excavation damage zones and excavation disturbed zones form near and far from the opening surfaces (Tsang et al. 2005), respectively.

In addition to field measurements, laboratory triaxial tests have widely been used to study the mechanical characteristics of sandstones (Wong and Baud 2012). Using triaxial tests, Weng et al. (2005) investigated the nonlinear elasticity, shear-induced dilatation, and plastic flow behaviours of Tertiary sandstone in Taiwan, Tsai et al. (2008) revealed that the associated flow rule is appropriate for describing the plastic and creep behaviour of a weak sandstone, while Zhang et al. (2020) evaluated the deformation, strength, and failure modes of a low-porosity sandstone under true triaxial-stress loading paths.

Sandstone usually displays a failure behaviour between brittleness and ductility in the post-peak region (Wong and Baud 2012). Researchers have used the spatial acoustic emission (Yang et al. 2012), CT scanning (Yang et al. 2020), and digital imaging techniques (Song et al. 2013; Yin and Yang 2018) to observe and evaluate the damage process that develops in sandstone rocks. Through these experimental techniques, microscopic fracturing mechanisms have been revealed, and linked to compaction localization (Baud et al. 2004) and formation of compaction bands (Townend et al. 2008).

Other experimental studies revealed that the cyclic stress paths have effects on the mechanical properties of sandstone. For instance, Geranmayeh Vaneghi et al. (2018), and Bagde and Petroš (2005) used uniaxial cyclic loading–unloading

tests to study the dependency of mechanical properties of sandstones on the uniaxial cyclic stress paths. Jia et al. (2018) used triaxial cyclic loading–unloading tests to study the evolution of elastic modulus, Poisson's ratio and crack damage stress with irreversible strains.

However, under constant confining pressure, the triaxial monotonic or cyclic loading–unloading stress paths differ significantly from the stress redistribution of underground excavation. A more realistic triaxial stress path would be to increase the axial pressure while simultaneously reducing the confining pressure. This, thus, is the focus of this experimental study.

In this study, to investigate the fundamental characteristics of a sandstone material, triaxial tests (at constant and reducing confining pressure, respectively) were performed by varying confining pressures from 0 to 50 MPa. The emphasis of this research is on investigating: (1) the effects of confining pressure on elastic constants, post-peak ductile/brittle deformations, and failure modes; (2) nonlinear characteristic of strength behaviour and yield surfaces; and (3) determination of the applicability of the associated or non-associated flow rules for describing its plastic behaviour.

2 Experiment Program

2.1 Sandstone Samples

The sandstone used in this study was sampled from Yunnan Province, China. The colour of the sandstone is grey. It has no obvious bedding structure and can be considered as an isotropic rock material. In this research, 11 cylindrical sandstone samples were used for testing. Their geometric and physical parameters were measured, and are presented in Table 1.

2.2 Test Apparatus

The experiments were carried out using a triaxial test apparatus, with a frame stiffness of 4×10^8 N/m, which can apply the maximum axial load of 1000 kN and 60 MPa of confining pressure, respectively. The test apparatus provides two LVDT micrometres and a circle-spring extensometer to measure the axial and circumferential deformation of the rock sample, respectively. The axial and circumferential strains can be calculated from these measurements by dividing the axial and circumferential displacement increments by the initial height and circumference of the rock sample, respectively.

Table 1 Geometric and physical parameters of the sandstone samples

| Sample no. | m/g | D/mm | H/mm | $\rho/kg\ m^{-3}$ | 1st σ_3/MPa | Stress path |
|------------|--------|--------|--------|-------------------|--------------------|---------------------|
| Su_1 | 481.41 | 50.03 | 100.03 | 2.45 | 0 | Constant σ_3 |
| Sc_1 | 486.83 | 50.04 | 100.02 | 2.48 | 10 | Constant σ_3 |
| Sc_2 | 483.26 | 50.04 | 100.00 | 2.46 | 20 | Constant σ_3 |
| Sc_3 | 487.78 | 50.05 | 100.04 | 2.48 | 30 | Constant σ_3 |
| Sc_4 | 483.13 | 50.03 | 100.01 | 2.46 | 40 | Constant σ_3 |
| Sc_5 | 484.47 | 50.03 | 100.05 | 2.46 | 50 | Constant σ_3 |
| Sr_1 | 482.67 | 50.02 | 100.05 | 2.46 | 10 | Reducing σ_3 |
| Sr_2 | 488.18 | 50.05 | 100.03 | 2.48 | 20 | Reducing σ_3 |
| Sr_3 | 484.99 | 50.04 | 100.02 | 2.47 | 30 | Reducing σ_3 |
| Sr_4 | 478.17 | 50.05 | 100.04 | 2.43 | 40 | Reducing σ_3 |
| Sr_5 | 484.18 | 50.03 | 100.05 | 2.46 | 50 | Reducing σ_3 |

m mass of rock sample, D diameter of rock sample, H height of rock sample, ρ density of rock sample, σ_3 confining pressure

2.3 Stress-Loading Procedures

In this study, triaxial compression tests were conducted under two different confinement conditions: constant and reducing confining pressure, abbreviated to CCP and RCP, respectively. To investigate the unloading characteristics of deep underground excavation (about 2000 m), high confining pressures ($\sigma_3=40$ and 50 MPa) are adopted in the CCP and RCP triaxial tests.

Figure 1a shows the stress-loading path of the CCP triaxial tests, which consists of two stages. In the $O \rightarrow t_1$ stage, the hydrostatic pressure, p_c , increases at a rate of 2.5 MPa/min, until it reaches the initial confining pressures (1st $\sigma_3 = 0, 10, 20, 30, 40$ and 50 MPa). Subsequently, in the $t_1 \rightarrow t_2$ stage, the axial stress σ_1 is applied to the rock sample using the axial-displacement control mode at a rate of 0.02 mm/min, while σ_3 is kept constant. When the rock sample fails, and the deviatoric stress, $q = \sigma_1 - \sigma_3$, drops to the residual strength value, q_r , the test is stopped.

Figure 1b shows that an RCP test comprises a series of loading stages. In the $O \rightarrow t_1$ stage, p_c is applied at a rate of

2.5 MPa/min until it reaches the initial confining pressures (1st $\sigma_3 = 10, 20, 30, 40$ and 50 MPa). In the $t_1 \rightarrow t_2$ stage, axial-displacement control mode is adopted to apply σ_1 to the rock sample at a rate of 0.02 mm/min. In the $t_1 \rightarrow t_2$ stage, the confining pressure is kept constant and equal to the 1st σ_3 . In the $t_2 \rightarrow t_3$ stage, when q approaches $0.5q_{p,c}$ ($t = t_2$, and $q_{p,c}$ is the peak strength measured in the CCP test), the confining pressure is decreased at a rate of 0.5 MPa/min, until the rock sample fails at $q_{f,r}$ ($t = t_3$). In the $t_3 \rightarrow t_4$ stage, the confining pressure is kept constant and equal to the 2nd σ_3 , while q approaches the 2nd residual strength, $q_{r,r}$ ($t = t_4$). Finally, in the $t_4 \rightarrow t_5$ stage, the confining pressure decreases at a rate of 0.5 MPa/min.

3 Experimental Results

3.1 Stress–Strain Relationships

Figure 2 displays the deviatoric stress–strain curves of the sandstone samples in the CCP and RCP tests. In the pre-peak

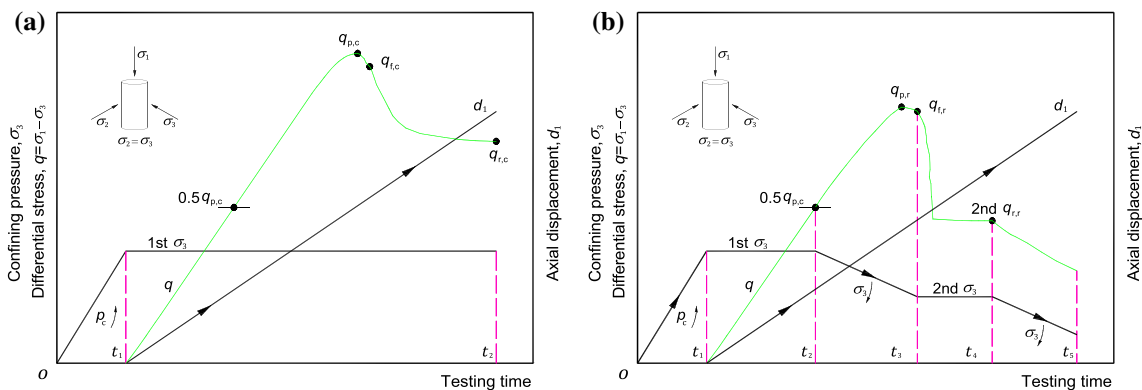


Fig. 1 Experimental stress-loading paths: **a** CCP triaxial compression test, and **b** RCP compression triaxial test

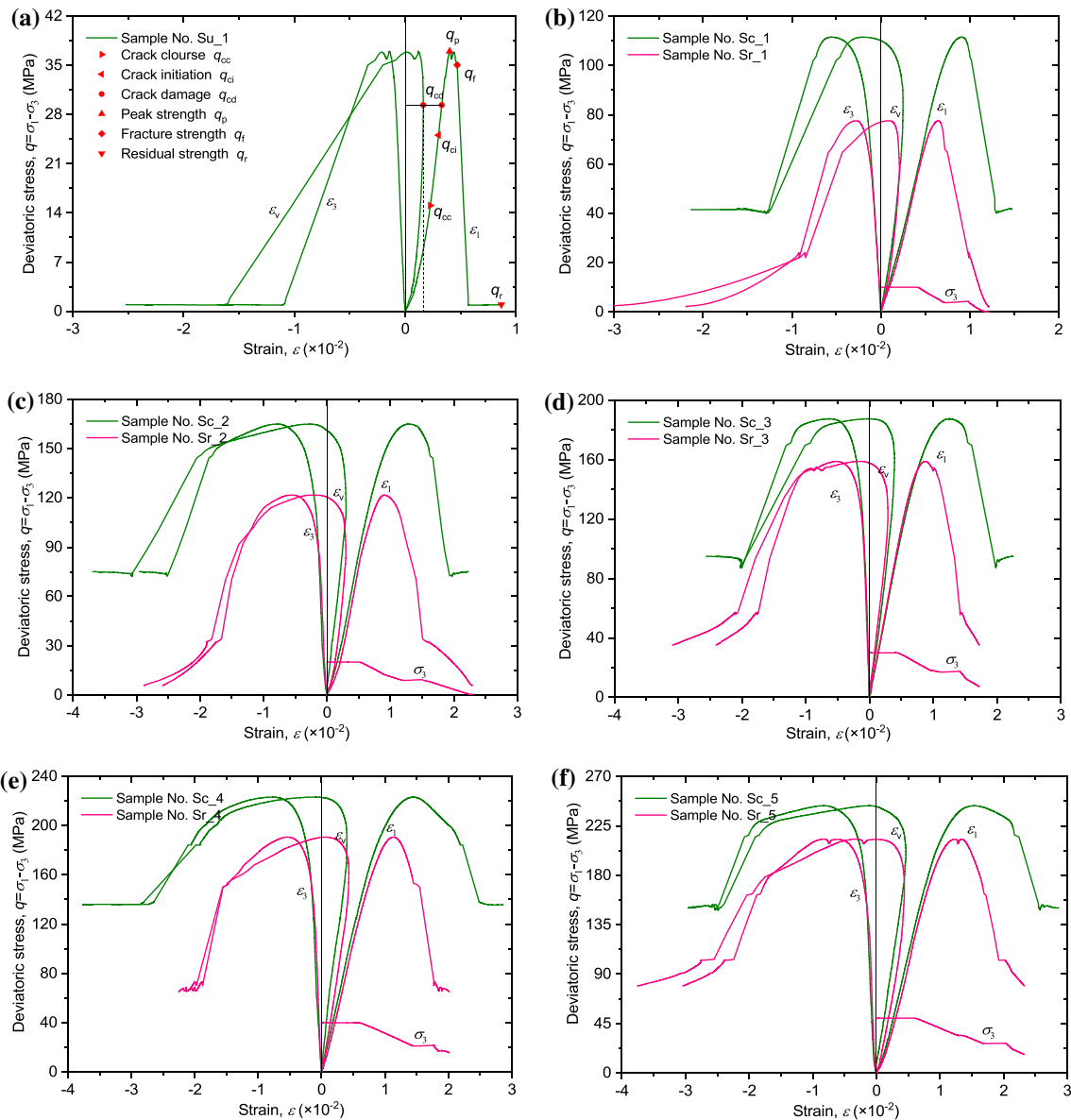


Fig. 2 Triaxial deviatoric stress–strain curves in CCP and RCP tests: **a** uniaxial compression test, **b** 1st $\sigma_3 = 10$ MPa, **c** 1st $\sigma_3 = 20$ MPa, **d** 1st $\sigma_3 = 30$ MPa, **e** 1st $\sigma_3 = 40$ MPa, and **f** 1st $\sigma_3 = 50$ MPa

region, the curves can be divided into four stages according to four threshold stresses. They are the initial crack closure stress, q_{cc} , crack initiation stress, q_{ci} , crack damage stress, q_{cd} , and peak strength, q_p , respectively (Cai et al. 2004), as shown in Figs. 2a and 3. The four stages are as follows:

1. Stage I (from O to q_{cc} , microcrack closure): The sandstone shows a nonlinear deformation, which is attributed to the closure of pre-existing microcracks and micropores with increasing deviatoric stress.
2. Stage II (from q_{cc} to q_{ci} , linear elastic deformation): The sandstone exhibits linear deformations. The stress and

strain data in this deformation stage can be utilized to determine the elastic constants.

3. Stage III (from q_{ci} to q_{cd} , microcrack initiation and stable microcrack growth): The sandstone exhibits a nonlinear deformation. During this stage, new microcracks initiate and propagate slowly and stably.
4. Stage IV (from q_{cd} to q_p , microcrack damage and unstable microcrack growth): The sandstone shows a nonlinear deformation, which is attributed to the unstable propagation of the newly developing microcracks. Beyond q_{cd} , the continuous increase in q leads to a transformation of the volumetric strain from contraction to dilatation.

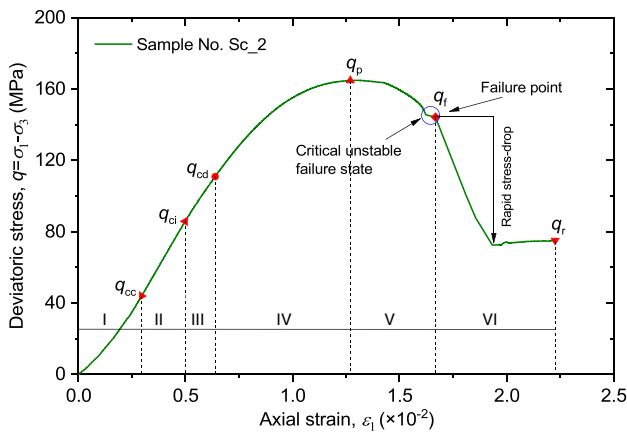


Fig. 3 Six stages of deformation in CCP test with constant confining pressure of 20 MPa

In all of the CCP and RCP tests, it is observed that the sandstone samples do not fail at the peak strength, q_p , but rather at q_f , which is used to identify the fracture strength. Because of the non-coincidence of q_f and q_p , the post-peak region can be divided into two stages as follows:

1. Stage V (from q_p to q_f , progressive failure): with the unstable propagation and coalescence of microcracks, the sandstone material undergoes a progressive failure, and displays a ductile deformation accompanied by a slow stress degradation.
2. Stage VI (from q_f to q_r , total failure and cohesion loss): as shown in Fig. 2, when the sandstone fails at q_f , q drops sharply, and the strains rise swiftly. Then, q remains stable, and the sandstone enters the residual strength in the CCP tests. However, in the RCP tests, q

diminish continuously when the confining pressure is gradually reduced.

It is worth noting that, in the post-peak region, the development of localized deformation causes the inhomogeneity of stress and strain in rock. In particular, when the stress reaches q_f , rupture occurs and the sandstone sample is broken into many fragments. Thus, it is more difficult to describe the mechanical behaviour of the sandstone with such mechanical quantities as stress and strain in stage VI. It is better to use the "force versus displacement" curves. But this will complicate the data representation in Fig. 2. Thus, the stress–strain quantities are still used in this research. However, the localization and discontinuous deformation of rocks are still worthy of attention in the post-peak region.

3.2 Characteristic Strengths

The four stress states (q_{cd} , q_p , q_f , and q_r) describe the characteristic strengths of the sandstone, which are presented in Table 2. To describe the strength of sandstone, the Mohr–Coulomb (MC) and Hoek–Brown (HB) failure criteria are applied to fit the data pairs $[\sigma_3, \sigma_{1,cd}]$, $[\sigma_3, \sigma_{1,p}]$, $[\sigma_3, \sigma_{1,f}]$, and $[\sigma_3, \sigma_{1,r}]$ ($\sigma_1 = q + \sigma_3$), as plotted in Fig. 4. In the $\sigma_3 - \sigma_1$ plane, the MC failure criterion is expressed as follows:

$$\sigma_1 = k_\varphi \sigma_3 + \sigma_u = \frac{1 + \sin \varphi}{1 - \sin \varphi} \sigma_3 + \frac{2c \cos \varphi}{1 - \sin \varphi}, \tag{1}$$

where c and φ is the cohesion and internal friction angle, respectively. $\sigma_u = (2c \cos \varphi)/(1 - \sin \varphi)$ denotes the characteristic strength under the uniaxial compressive state.

In the $\sigma_3 - \sigma_1$ plane, the HB criterion can be written as follows (Hoek and Brown 1997):

Table 2 Characteristic strength states of the tested sandstone material

| Sample no. | Crack damage stress state | | Peak strength state | | Fracture strength state | | Residual strength state | |
|------------|---------------------------|---------------|---------------------|------------|-------------------------|------------|-------------------------|------------|
| | σ_3 /MPa | q_{cd} /MPa | σ_3 /MPa | q_p /MPa | σ_3 /MPa | q_f /MPa | σ_3 /MPa | q_r /MPa |
| Su_1 | 0 | 29.32 | 0 | 37.00 | 0 | 35.04 | 0 | 0.94 |
| Sc_1 | 10.01 | 84.61 | 10.01 | 111.50 | 10.05 | 102.08 | 10.01 | 41.11 |
| Sc_2 | 20.00 | 110.62 | 20.12 | 164.87 | 20.22 | 144.21 | 20.08 | 74.20 |
| Sc_3 | 30.00 | 160.15 | 30.01 | 187.54 | 30.04 | 169.69 | 30.00 | 94.86 |
| Sc_4 | 40.03 | 183.14 | 40.11 | 223.10 | 40.13 | 184.07 | 40.09 | 135.61 |
| Sc_5 | 50.00 | 209.39 | 50.01 | 243.28 | 50.03 | 215.08 | 50.00 | 150.15 |
| Sr_1 | 9.98 | 58.44 | 5.16 | 77.57 | 3.76 | 64.74 | 3.49 | 22.50 |
| Sr_2 | 18.10 | 98.08 | 12.41 | 121.62 | 8.94 | 102.38 | 8.70 | 32.94 |
| Sr_3 | 26.01 | 137.15 | 20.11 | 158.81 | 16.98 | 135.30 | 16.27 | 56.88 |
| Sr_4 | 35.98 | 160.90 | 28.34 | 190.61 | 21.16 | 150.09 | 18.99 | 70.97 |
| Sr_5 | 43.57 | 181.25 | 34.26 | 212.90 | 26.74 | 161.92 | 26.41 | 100.78 |

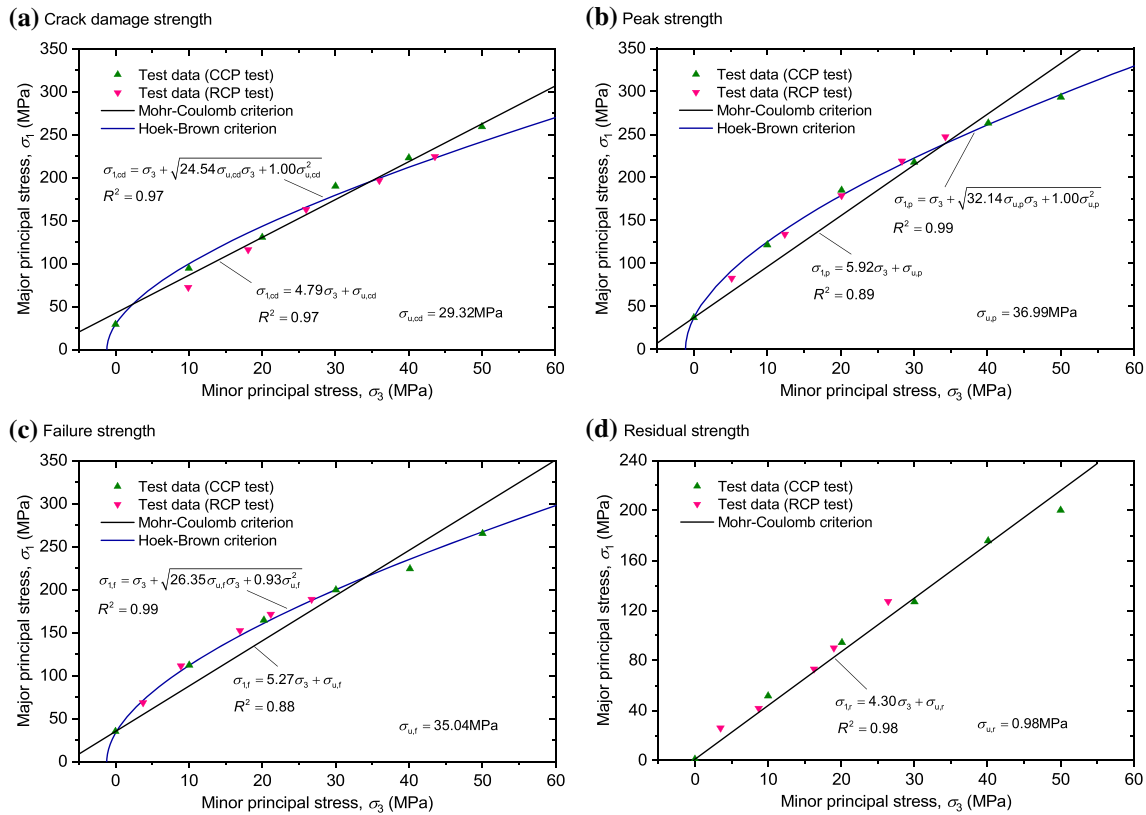


Fig. 4 Characteristic strength states of the sandstone in CCP and RCP tests: **a** crack damage strength, **b** peak strength, **c** failure strength, and **d** residual strength

$$\sigma_1 = \sigma_3 + \sqrt{m\sigma_u\sigma_3 + s\sigma_u^2} \quad (2)$$

where m and s are the two strength parameters for the HB criterion.

It can be observed from Fig. 4a that the MC and HB criteria can reflect the changes in crack damage strength, $\sigma_{1,cd}$, with the confining pressure, σ_3 . For the prediction of the peak and failure strengths (Fig. 4b, c), the modelling results of the HB criterion are much better than those of the MC criterion. Figure 4d demonstrates that the relationship between $\sigma_{1,r}$ and σ_3 is strictly linear, meaning that only the

MC criterion can be adopted to model the residual strength behavior of the sandstone.

Corresponding to Fig. 4, the characteristic strength parameters for the MC and HB criteria are calculated and summarised in Table 3. It is found that before failure, the value of cohesion, c , varies slightly, ranging from 6.70 to 7.63 MPa, with a relative increase of 13.9%. However, after the sandstone samples fail, the cohesion is reduced to an extremely small residual value of 0.23 MPa, i.e., a relative loss of 96.6%.

In the pre-peak region, the strain-hardening effect gradually increases the value of friction angle φ , from 40.9° at q_{cd} to 45.3° at q_p , respectively, with a relative rise of 10.8%.

Table 3 Characteristic strength parameters of the sandstone for the Mohr–Coulomb and Hoek–Brown strength criteria

| Characteristic strength states | UCCS | Mohr–Coulomb failure criterion | | Hoek–Brown failure criterion | |
|--------------------------------|-------|--------------------------------|-------------------|------------------------------|------|
| | | σ_u /MPa | Cohesion c /MPa | Friction angle φ | m |
| Crack damage | 29.32 | 6.70 | 40.9° | 24.54 | 1.00 |
| Peak strength | 36.99 | 7.60 | 45.3° | 32.14 | 1.00 |
| Failure strength | 35.03 | 7.63 | 42.9° | 26.35 | 0.93 |
| Residual strength | 0.98 | 0.23 | 38.5° | – | – |

UCCS Uniaxial compressive characteristic strength

In the post-peak region from q_p to q_f , φ gradually decreases from 45.3 to 42.9° , i.e., a relative reduction of 5.3% . When the sandstone samples fail completely beyond q_f , φ diminishes to the residual value of 38.5° (with a relative loss of 15.0%), which is the friction angle between the fracture surfaces.

4 Elastoplastic Deformation Behaviour

To examine the elastoplastic deformation of the sandstone, the total strain tensor should be decomposed into two components:

$$\epsilon_{ij} = \epsilon_{ij}^e + \epsilon_{ij}^p, \tag{3}$$

where ϵ_{ij} , ϵ_{ij}^e and ϵ_{ij}^p are the total, elastic and plastic strain tensors, respectively. To separate the strains, the elastic constants of the sandstone should be measured first.

4.1 Elastic Constants

The straight line segments from q_{cc} to q_{ci} in the deviatoric stress–strain curves (Fig. 2) are adopted to calculate the elastic modulus E and Poisson’s ratio ν of the sandstone using the following formula:

$$E = \frac{q_{ci} - q_{cc}}{\epsilon_{1,ci} - \epsilon_{1,cc}} \text{ and } \nu = -\frac{\epsilon_{3,ci} - \epsilon_{3,cc}}{\epsilon_{1,ci} - \epsilon_{1,cc}}, \tag{4}$$

The experimental data corresponding to the q_{cc} and q_{ci} stress states and the computed results of E and ν are given in Table 4. Figure 5 shows that the confining pressure has a significant effect on the elastic constants. When σ_3 raises from 0 to 20 MPa, E increases quickly from 13.05 to 20.60 GPa, with a relative increase of 57.9% . However, when σ_3 is greater than 20 MPa, E increases only to an average value

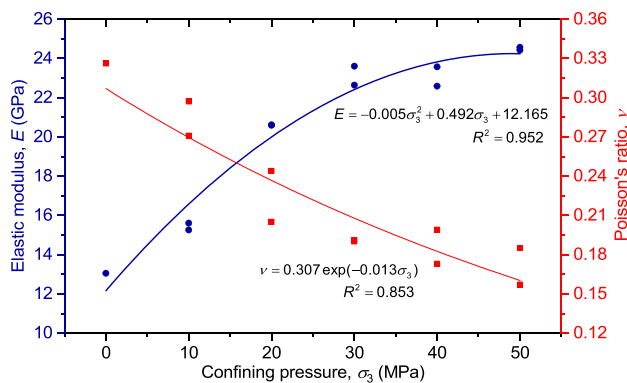


Fig. 5 Elastic modulus and Poisson’s ratio of the sandstone, which are varying as a function of the confining pressure

of 23.56 GPa, i.e., by 14.4% . Under uniaxial compressive stress, the value of ν is about 0.33, but with an increase in σ_3 , ν decreases nonlinearly to 0.17 at the confining pressure of 50 MPa, i.e., by 48.5% .

4.2 Plastic Behaviour

4.2.1 Plastic Shear and Volumetric Strains

Using the elastic constants presented in Table 4, the elastic strains ϵ_{ij}^e can be computed. By subtracting ϵ_{ij}^e from the total strain ϵ_{ij} , the plastic strain ϵ_{ij}^p can be calculated. Furthermore, the strain tensor can be divided into two parts, which are shear strain γ_s and volumetric strain ϵ_v . In the conventional triaxial compression test ($\sigma_2 = \sigma_3$ and $\epsilon_2 = \epsilon_3$), γ_s and ϵ_v can be expressed as follows:

$$\gamma_s = \frac{2}{3}(\epsilon_1 - \epsilon_3) \text{ and } \epsilon_v = 2\epsilon_3 + \epsilon_1. \tag{5}$$

Table 4 Calculation of elastic constants of the sandstone samples

| Sample no. | Confining pressure σ_3 /MPa | Crack closure state | | | Crack initiation state | | | Elastic constants | |
|------------|---------------------------------------|----------------------|----------------------|---------------|------------------------|----------------------|---------------|-------------------|-------|
| | | $\epsilon_{3,cc}/\%$ | $\epsilon_{1,cc}/\%$ | q_{cc} /MPa | $\epsilon_{3,ci}/\%$ | $\epsilon_{1,ci}/\%$ | q_{ci} /MPa | E /GPa | ν |
| Su_1 | 0 | -0.05 | 0.23 | 15.05 | -0.06 | 0.28 | 22.07 | 13.05 | 0.33 |
| Sc_1 | 10 | -0.05 | 0.23 | 30.04 | -0.09 | 0.36 | 50.05 | 15.26 | 0.27 |
| Sc_2 | 20 | -0.08 | 0.27 | 37.81 | -0.12 | 0.45 | 76.62 | 20.59 | 0.21 |
| Sc_3 | 30 | -0.03 | 0.21 | 47.04 | -0.07 | 0.40 | 88.90 | 22.64 | 0.19 |
| Sc_4 | 40 | -0.06 | 0.21 | 48.04 | -0.11 | 0.47 | 109.27 | 23.57 | 0.20 |
| Sc_5 | 50 | -0.07 | 0.25 | 46.36 | -0.12 | 0.54 | 117.10 | 24.42 | 0.19 |
| Sr_1 | 10 | -0.05 | 0.23 | 27.00 | -0.09 | 0.37 | 48.51 | 15.61 | 0.30 |
| Sr_2 | 20 | -0.06 | 0.29 | 34.77 | -0.11 | 0.50 | 78.68 | 20.61 | 0.24 |
| Sr_3 | 30 | -0.04 | 0.22 | 50.00 | -0.07 | 0.37 | 85.10 | 23.60 | 0.19 |
| Sr_4 | 40 | -0.05 | 0.26 | 50.03 | -0.09 | 0.54 | 112.38 | 22.58 | 0.17 |
| Sr_5 | 50 | -0.06 | 0.30 | 48.14 | -0.11 | 0.61 | 124.88 | 24.57 | 0.16 |

4.2.2 Plastic Strain Increment

Once the plastic shear strain, γ_s^p , and the plastic volumetric strain, ε_v^p , are obtained, the plastic flow of the sandstone can be described with the plastic strain increment vector. The magnitude of plastic strain increment, $d\varepsilon^p$, is defined as follows:

$$d\varepsilon^p = \sqrt{(d\gamma_s^p)^2 + (d\varepsilon_v^p)^2}, \tag{6}$$

where $d\gamma_s^p$ and $d\varepsilon_v^p$ represent the plastic shear and volumetric strain increment, respectively.

Figure 6 shows how the magnitude of the plastic strain increment, $d\varepsilon^p$, varies with testing time in the CCP and RCP

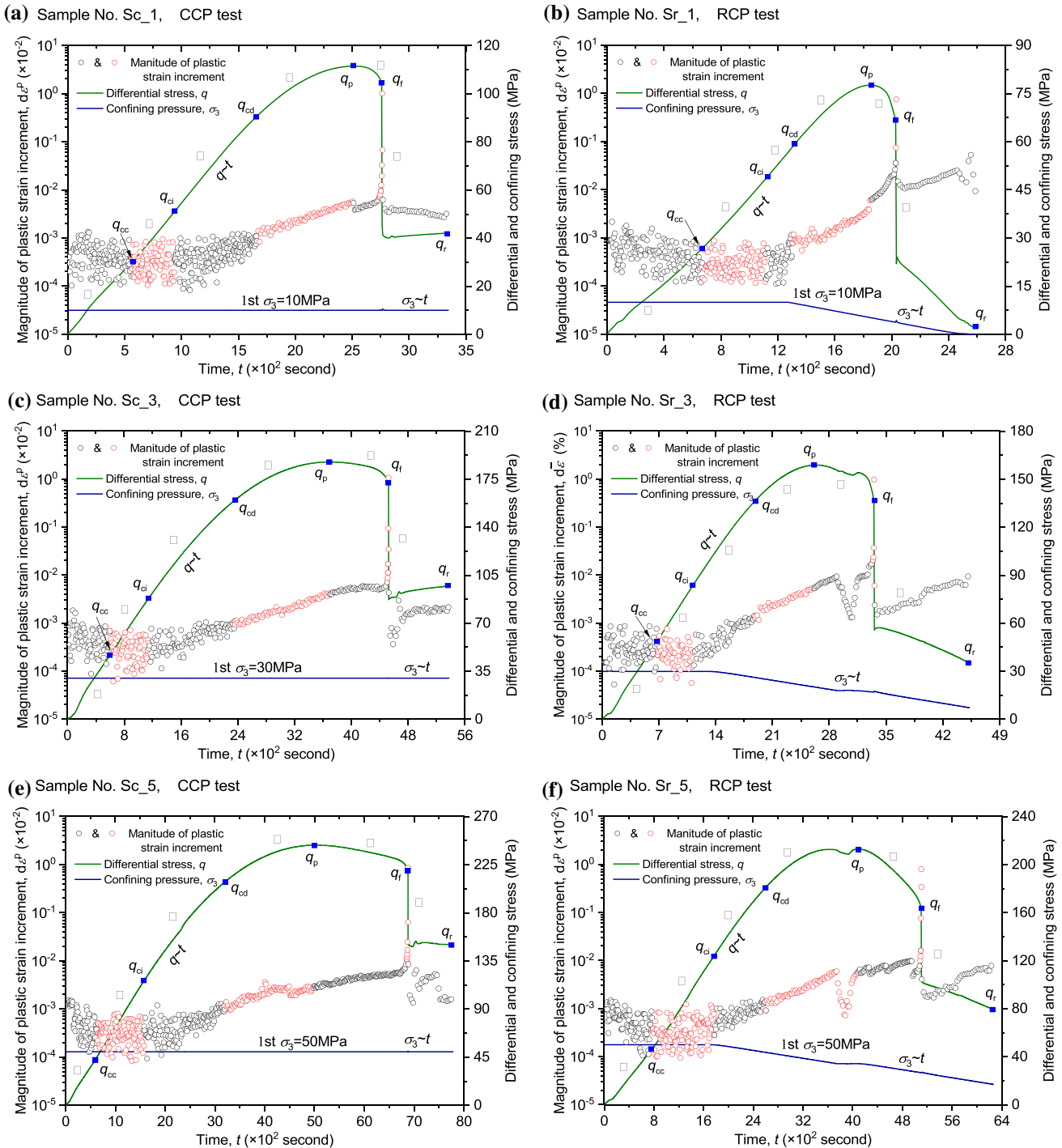


Fig. 6 Evolution of plastic strain increment of the sandstone samples in two different CCP and RCP tests

tests. It can be observed that in the deformation stages I–III ($q < q_{cd}$), $d\epsilon^p$ changes from 10^{-6} to 10^{-5} , while in stages IV and V it increases regularly from 10^{-5} to 10^{-4} . When q approaches q_f , $d\epsilon^p$ raises faster. When the sandstone samples fail completely after reaching q_f in the CCP and the RCP tests, $d\epsilon^p$ soars sharply to the peak values (about 10^{-2}), and then falls rapidly toward the stable values of the residual deformation stage. Overall, the peak values in the RCP test conditions are greater than those in the CCP tests.

By comparing the CCP test results (Fig. 6a, c, and e), it can be seen that with the increase in σ_3 from 10 to 50 MPa, the growth rate of the plastic strain increment slows down. A similar phenomenon is also observed in the RCP tests by comparing Fig. 6b, d and f. It is also be found that in the RCP tests, unloading of the confining pressure results in greater increases in the plastic strain than in the CCP tests.

4.2.3 Plastic Flow Direction

The direction of the plastic strain increment vector (i.e. plastic flow) can be described using the plastic flow angle ψ , which is defined as follows (Tsai et al. 2008):

$$\tan \psi = \frac{d\gamma_s^p}{d\epsilon_v^p} \tag{7}$$

The plastic flow angle ψ ranges from 0° to 180° . When $0^\circ \leq \psi < 90^\circ$, $d\epsilon_v^p$ is compressive. When $\psi > 90^\circ$, $d\epsilon_v^p$ is dilative. Moreover, $\psi = 90^\circ$ suggests a transition of the plastic volumetric deformation from contraction to dilatation.

Based on the analysis of the plastic flow angle, ψ , the shear-induced dilatation behaviour of the sandstone can be investigated in the $p - q$ stress plane, where $p = (\sigma_1 + 2\sigma_3)/3$ is the mean stress.

As far as the plasticity is concerned, the MC and HB criterion curves obtained by fitting the characteristic strength

data are generally called the yield surfaces (Fig. 4). These yield surfaces can alternatively be described using $q = 6(p \sin \varphi + c \cos \varphi)/(3 - \sin \varphi)$ for the MC failure criterion, and $q = (-m\sigma_u + \sqrt{m^2\sigma_u^2 + 36m\sigma_u p + 36s\sigma_u^2})/6$ for the HB failure criterion, respectively, as plotted in Figs. 7 and 8. Additionally, these yield surfaces passing through the stress states of q_{cd} , q_p , q_f , and q_r are generally referred to as the initial, ultimate, fracture, and residual yield surfaces, respectively.

The plastic flow directions variations along the CCP and RCP stress paths are displayed in Figs. 7 and 8, respectively. Figure 8 marks the intersection points (S_{cd} , S_p , S_f , and S_r) of the stress paths and the failure surfaces, and a summary of the average values of ψ near these intersection points is presented in Table 5. By substituting the stress states at the intersection points into Eqs. (9) and (10), the tangent angles, α , of the yield surface can be computed, as presented in Table 5.

Figures 7 and 8, and Table 5 show that in the pre-peak region (Figs. 7a and 8a), when stress levels are lower, the plastic flow directions are disorganized, however, when the stress levels increase and approach the yield surfaces, the plastic flow directions tend to be within the range of $90^\circ < \psi < 180^\circ$. Figures 7b and 8b show that in the post-peak region ψ is always greater than 90° , implying that the sandstone undergoes a plastic volume dilatation.

It is observed that at the intersection points the difference $\psi - \alpha$ on these yield surfaces is in the range from 84.3 to 88.3° . This demonstrates that when the stress reaches the yield states, the plastic flow directions are predominantly perpendicular to the yield surfaces. Because $\psi - \alpha$ is very close to 90° , the associated flow rule is suitable for describing the plastic behavior of the sandstone.

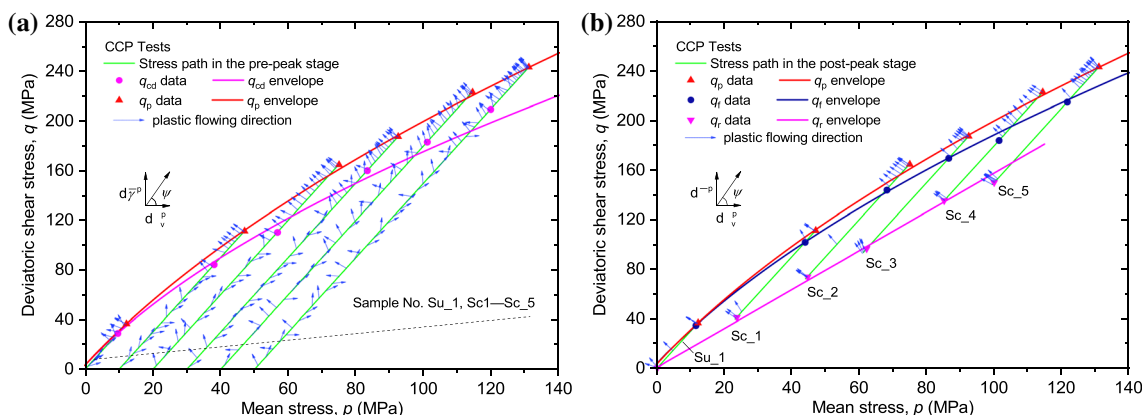


Fig. 7 Characteristic strength envelopes and the plastic flow directions of the sandstone in CCP tests: a testing results in pre-peak region, and b testing results in post-peak region

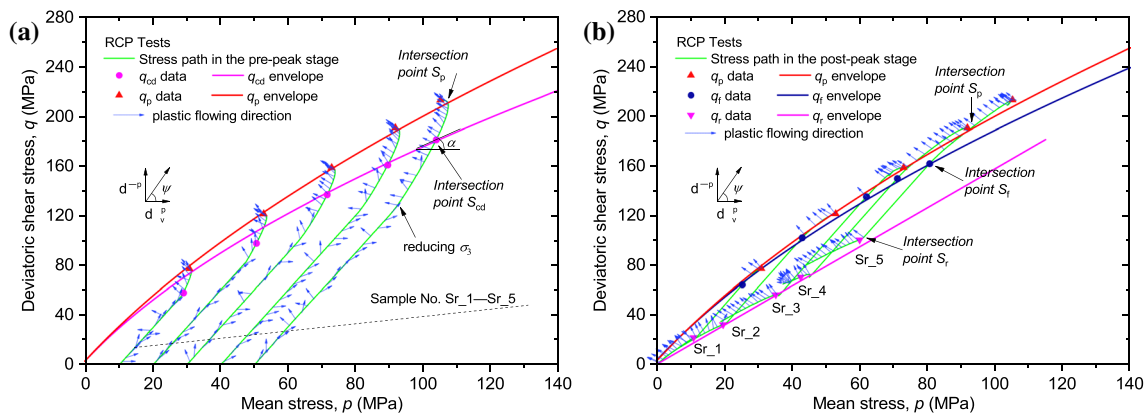


Fig. 8 Characteristic strength envelopes and the plastic flow directions of the sandstone in RCP tests: **a** testing results in pre-peak region, and **b** testing results in post-peak region

Table 5 Summary of the plastic flow directions at the intersection points of the stress paths and failure surfaces

| Sample no. | Intersection point S_{cd} | | | Intersection point S_p | | | Intersection point S_f | | | Intersection point S_r | | |
|------------|-----------------------------|-----------------|------------------------|--------------------------|-----------------|------------------------|--------------------------|-----------------|------------------------|--------------------------|-----------------|------------------------|
| | $\psi/^\circ$ | $\alpha/^\circ$ | $\psi - \alpha/^\circ$ | $\psi/^\circ$ | $\alpha/^\circ$ | $\psi - \alpha/^\circ$ | $\psi/^\circ$ | $\alpha/^\circ$ | $\psi - \alpha/^\circ$ | $\psi/^\circ$ | $\alpha/^\circ$ | $\psi - \alpha/^\circ$ |
| Su_1 | 157.6° | 67.4° | 90.2° | 152.0° | 68.3° | 83.7° | 158.6° | 67.8° | 90.8° | 162.3° | 57.5° | 104.8° |
| Sc_1 | 146.1° | 60.1° | 86.0° | 145.7° | 62.2° | 83.5° | 145.2° | 62.7° | 82.5° | 140.6° | 57.5° | 83.1° |
| Sc_2 | 142.2° | 56.6° | 85.6° | 144.6° | 58.5° | 86.1° | 145.9° | 57.1° | 88.8° | 146.4° | 57.5° | 88.9° |
| Sc_3 | 140.5° | 52.7° | 87.8° | 147.8° | 56.5° | 91.3° | 134.9° | 54.7° | 80.2° | 134.7° | 57.5° | 80.2° |
| Sc_4 | 139.5° | 50.5° | 89.0° | 147.5° | 54.4° | 93.1° | 135.6° | 53.3° | 82.3° | 147.5° | 57.5° | 90.0° |
| Sc_5 | 135.6° | 48.5° | 87.1° | 134.8° | 52.9° | 81.9° | 139.9° | 51.0° | 88.9° | 142.8° | 57.5° | 85.3° |
| Sr_1 | 149.1° | 62.1° | 87.0° | 146.4° | 64.8° | 81.6° | 146.6° | 66.0° | 80.6° | 156.0° | 57.5° | 98.5° |
| Sr_2 | 144.3° | 57.3° | 87.0° | 144.1° | 61.3° | 82.8° | 145.4° | 61.0° | 84.4° | 142.0° | 57.5° | 84.5° |
| Sr_3 | 141.8° | 55.1° | 86.7° | 148.5° | 58.7° | 89.8° | 141.4° | 59.8° | 81.6° | 140.4° | 57.5° | 82.9° |
| Sr_4 | 137.5° | 51.9° | 85.6° | 143.6° | 56.6° | 87.0° | 143.1° | 57.9° | 85.2° | 146.3° | 57.5° | 88.8° |
| Sr_5 | 142.5° | 50.2° | 92.3° | 146.3° | 55.2° | 91.1° | 139.2° | 56.8° | 82.4° | 142.2° | 57.5° | 84.7° |

5 Post-Peak Failure Characteristics

5.1 Method of Brittleness Evaluation

In general, the post-peak instability of rocks can be categorized into two classes, referred to as Class I and Class II, respectively (Tarasov and Stacey, 2017). The stress–strain curves (Fig. 2) demonstrates that the post-peak behaviour of the studied sandstone can be regarded as Class I. To evaluate the brittleness of the sandstone, the following discussion introduces the brittleness criterion proposed by Tarasov and Potvin (2013).

According to Tarasov and Potvin (2013), during the post-peak failure process the deviatoric stress degrades, following the path between points A and B (shown in Fig. 9). The elastic energy at points A and B can be represented with the areas of right-angled triangles $\triangle ACE$ and $\triangle BDF$,

respectively. The elastic energy, ΔW_{A-B}^e , released by the rock specimen can be expressed as follows:

$$\Delta W_{A-B}^e = W_A^e - W_B^e = \frac{q_A^2 - q_B^2}{2E}, \tag{8}$$

where $E = dq/d\epsilon_1$ is the elastic modulus. The area of quadrilateral AEFB represents the additional energy, ΔW_{A-B}^a , which can be calculated using the following equation:

$$\Delta W_{A-B}^a = W_A^a - W_B^a = \frac{q_A^2 - q_B^2}{2M} \tag{9}$$

where $M = dq/d\epsilon_1$ denotes the post-peak modulus, which is shown in Fig. 9. According to energy balance, the post-peak rupture energy, ΔW_{A-B}^r , for transition between points A and B can be calculated as follows:

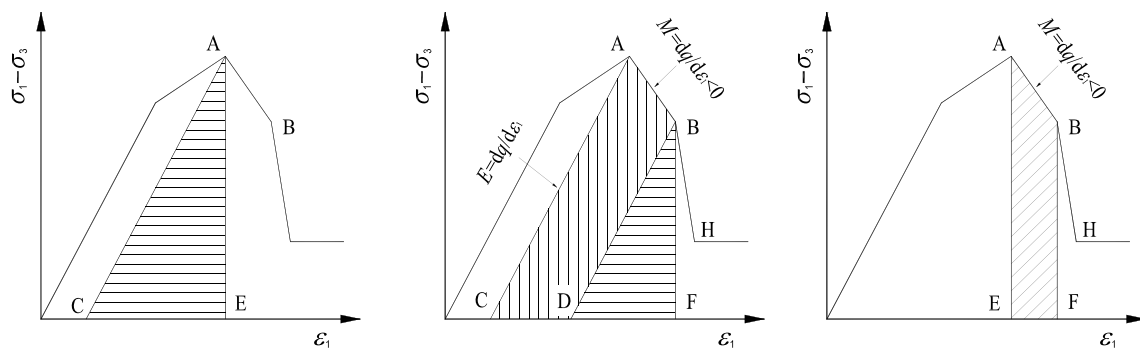


Fig. 9 An illustration that shows brittleness estimation based on the post-peak energy balance for rocks of Class I. In order to suit to the post-peak failure behavior of the studied sandstone, this diagram is

modified from Tarasov and Potvin (2013). Stress states at points A, B and H are in accordance with peak strength q_p , failure strength q_f and residual strength q_r

$$\Delta W_{A-B}^r = \Delta W_{A-B}^e - \Delta W_{A-B}^a = \frac{(q_A^2 - q_B^2)(M - E)}{2EM} \quad (10)$$

Tarasov and Potvin (2013) defined a brittleness index, B_r , as the ratio between the rupture energy and the released elastic energy as follows:

$$B_r = \frac{\Delta W_{A-B}^r}{\Delta W_{A-B}^e} = \frac{M - E}{2M} \quad (11)$$

In the study by Tarasov and Potvin (2013), the value of the brittleness index, B_r , ranges from 0 to $+\infty$. They linked “super brittleness” to $B_r = 0$, “brittleness” to $B_r = 1$, and “semibrittleness” to $B_r = 2$, respectively. With the rise in the value of the brittleness index, B_r , rock behaviour becomes more ductile.

5.2 Brittle Features of the Sandstone

The brittleness indices of the sandstone in the post-peak region (i.e., from q_p to q_f , or along the path $A \rightarrow B$, shown in Fig. 9) are presented in Table 6. In the CCP tests, the sandstone brittleness index ranges from 3.39 to 5.84, whereas in the RCP tests, between 2.24 and 4.14, respectively. This demonstrates that in the CCP and the RCP tests, the sandstone undergoes a ductile progressive failure, exhibiting a slow stress degradation from q_p to q_f .

The brittleness indices at the time of the complete failure (q_f , or along the path $B \rightarrow H$, shown in Fig. 9) are given in Table 6. In the CCP tests, the value of B_r at q_f is in a range of 1.47–2.14, while in the RCP tests, B_r ranges from 1.66 to 1.94, respectively. The CCP and RCP tests indicate that the sandstone experiences a semibrittle failure.

Table 6 also shows that in the CCP tests, the values of B_r at q_f tend to increase with rising confining pressure, however, in the RCP tests, the values of B_r at q_f decrease markedly. The reason may be that under greater confining

Table 6 Summary of the post-peak failure characteristics of the sandstone samples

| Sample no. | σ_3 /MPa (At q_p) | σ_3 /MPa (At q_f) | $B_r(q_p \rightarrow q_f)$ | B_r (At q_f) | Dip angle of rupture fracture $\beta/^\circ$ | Failure modes |
|------------|-----------------------------|-----------------------------|----------------------------|-------------------|--|-----------------------------|
| Su_1 | 0 | 0 | 3.82 | 1.47 | 76° | Tension-splitting failure |
| Sc_1 | 10.01 | 10.05 | 3.39 | 1.96 | 66° | Mixed tension-shear failure |
| Sc_2 | 20.12 | 20.22 | 5.53 | 1.87 | 64° | Mixed tension-shear failure |
| Sc_3 | 30.01 | 30.04 | 5.35 | 2.03 | 59° | Mixed tension-shear failure |
| Sc_4 | 40.11 | 40.13 | 5.11 | 2.14 | 55° | Shear failure |
| Sc_5 | 50.01 | 50.03 | 5.84 | 2.04 | 52° | Shear failure |
| Sr_1 | 5.16 | 3.76 | 2.24 | 1.91 | 70° | Mixed tension-shear failure |
| Sr_2 | 12.41 | 8.94 | 4.14 | 1.94 | 66° | Mixed tension-shear failure |
| Sr_3 | 20.11 | 16.98 | 3.78 | 1.81 | 64° | Mixed tension-shear failure |
| Sr_4 | 28.34 | 21.16 | 3.30 | 1.66 | 57° | Shear failure |
| Sr_5 | 34.26 | 26.74 | 2.53 | 1.71 | 54° | Shear failure |

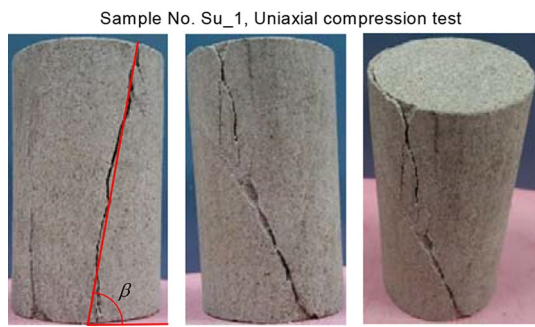


Fig. 10 Failure mode of the sandstone (Sample No. Su_1) under the uniaxial compression test

pressures, the unloading of confinement is favourable for a

more efficient transformation of the elastic energy released from the rock materials during rupture. This indirectly confirms that rocks subjected to high geostresses are commonly prone to more severe brittle failures during excavation unloading.

5.3 Failure Modes of the Sandstone

Figures 10 and 11 show the photographs of the failed sandstone samples, whose rupture properties are briefly described in Table 6. In uniaxial compression (Fig. 10), the sandstone behaviour follows a violent tension-splitting rupture that causes fragment-spalling damage at the cylindrical surface.

Figure 11 illustrates the influence of the confining pressure on the failure mode in the triaxial CCP and RCP tests.

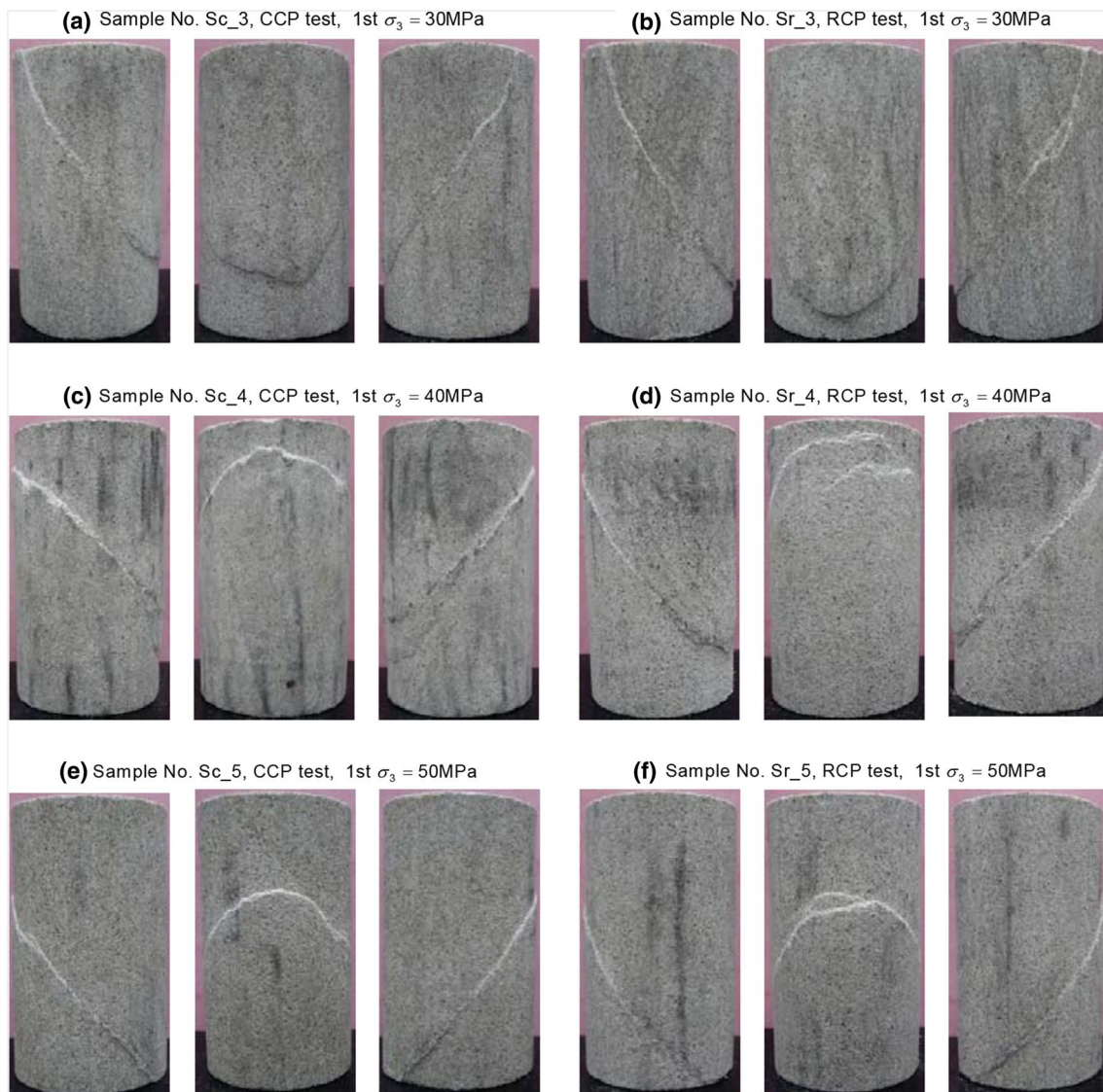


Fig. 11 Failure modes of the sandstone in the triaxial CCP and RCP tests

For low and intermediate confining pressures, as shown in Fig. 11a–f, the sandstone follows a mixed tension-shear failure. This is a transitional failure mode from the tension splitting to shear rupture. In general, each failed sample has a primary fracture passing through diagonally. Under the larger confining pressures, the sandstone tends to undergo a shear rupture, as illustrated in Fig. 11g–j. It is interesting to note that with rising confining pressure, the shear fractures become thinner, more planer and smoother.

As illustrated in Table 6, under uniaxial compression the dip angle, β , of the primary tensile fracture is about 76° . When the initial confining pressure rises to 30 MPa, β in the CCP tests reduces to approximately $59\text{--}66^\circ$. Meanwhile in the RCP tests, β is steeper, ranging from 64 to 70° . When the initial confining pressure reaches 40–50 MPa, β in the CCP and RCP tests decreases to $52^\circ\text{--}55^\circ$ and $54^\circ\text{--}57^\circ$, respectively. This suggests that the unloading of confining pressure influences β of the primary fracture.

6 Conclusions

This research scrutinized the mechanical characteristics of a sandstone material under the CCP and RCP triaxial testing conditions. Based on the experimental results, the following conclusions can be drawn:

1. The deviatoric stress–strain curves suggest that the sandstone deformation can be divided into six stages. In the post-peak region, due to the separation of the failure point from the peak stress, the sandstone moves through a ductile deformation stage (from q_p to q_f). The greater the confining pressure, the more distinct the ductile deformation stage. After the sandstone fails, it reaches a stable residual deformation.
2. The characteristic strength envelopes for q_{cd} , q_p , and q_f are nonlinear and can be described using the Hoek–Brown criterion. After the sandstone fails, its cohesion strength is completely lost. This means that its residual strength only comes from the friction angle of the fractures between the rock blocks. Thus, the residual strength behaviour of the sandstone can only be described using the linear Mohr–Coulomb criterion.
3. When the deviatoric stress is smaller than the crack damage strength, q_{cd} , the plastic strain increment is remarkably small. When the deviatoric stress increases beyond q_{cd} , the plastic strain begins to increase steadily. At the moment sandstone fails, the plastic strain increment surges to 10^{-2} . In general, the rising rate of the plastic strain in the RCP tests is comparatively faster than that in the CCP tests. This suggests that the unloading of the confining pressure accelerates the development of the plastic strain in the sandstone.
4. Under the CCP and RCP testing conditions, the sandstone exhibits the same characteristics in the plastic flow direction. When the deviatoric stress approaches the yield states, the angles between the plastic flow directions and tangent slopes of the yield surfaces range from 84.3 to 88.3° . This means that the associated flow rule can be employed to describe the plastic behavior of the sandstone.
5. With increasing confining pressure, the sandstone brittleness index rises gradually, however, when approaching the critical failure states, the index reduces to a value in the range of 1.47–2.14. This suggests that the post-peak failure behaviour of the sandstone shift with progressive stress degradation from ductile to semibrittle with a sharp stress drop.
6. In uniaxial compression, the sandstone is ruptured and shows a primary tension-splitting fracture with a dip angle $\beta = 75^\circ$. Under the low to intermediate confining pressures, the sandstone is ruptured in a mixed tension-shear failure mode, where a primary fracture passes through the sample diagonally with a dip angle ranging from 60 to 70° . Under the high confining pressures, the sandstone experiences a shear rupture in the failure mode, where a shear fracture cuts the sample obliquely with a dip angle in the range of $52\text{--}57^\circ$.

Acknowledgments The work presented in this paper were financially supported by the National Natural Science Foundation of China (Grant No. 12062026 and 51609070).

References

- Bagde MN, Petroš V (2005) The effect of machine behaviour and mechanical properties of intact sandstone under static and dynamic uniaxial cyclic loading. *Rock Mech Rock Eng* 38:59–67
- Baud P, Klein E, Wong T-f (2004) Compaction localization in porous sandstones: spatial evolution of damage and acoustic emission activity. *J Struct Geol* 26:603–624
- Cai M, Kaiser PK, Tasaka Y, Maejima T, Morioka H, Minami M (2004) Generalized crack initiation and crack damage stress thresholds of brittle rock masses near underground excavations. *Int J Rock Mech Min Sci* 41:833–847
- Geranmayeh Vaneghi R, Ferdosi B, Okoth AD, Kuek B (2018) Strength degradation of sandstone and granodiorite under uniaxial cyclic loading. *J Rock Mech Geotech Eng* 10:117–126
- Hoek E, Brown ET (1997) Practical estimates of rock mass strength. *Int J Rock Mech Min Sci* 34:1165–1186
- Jeng F-S, Weng M-C, Huang T-H, Lin M-L (2002) Deformational characteristics of weak sandstone and impact to tunnel deformation. *Tunn Undergr Sp Technol* 17:263–274
- Jia C, Xu W, Wang R, Wang W, Zhang J, Yu J (2018) Characterization of the deformation behavior of fine-grained sandstone by triaxial cyclic loading. *Constr Build Mater* 162:113–123
- Jiang Y, Wang LS (2002) Problems of high stress rock burst and water outburst and countermeasures in deep and long tunnels. *Chin J Rock Mechan Eng* 21:1319–1323 ((in Chinese))

- Li PX, Feng XT, Feng GL, Xiao YX, Chen BR (2019) Rockburst and microseismic characteristics around lithological interfaces under different excavation directions in deep tunnels. *Eng Geol* 260:105209
- Oliveira D, Diederichs MS (2017) Tunnel support for stress induced failures in Hawkesbury Sandstone. *Tunn Undergr Space Technol* 64:10–23
- Shang Y-J, Shi Y-Y, Zeng Q-L, Yin J-T, Xue J-H (2005) TBM jamming and deformation in complicated geological conditions and engineering measures. *Chin J Rock Mech Eng* 24:3858–3863 (in Chinese)
- Soleiman Dehkordi M, Shahriar K, Moarefvand P, Gharouninik M (2013) Application of the strain energy to estimate the rock load in squeezing ground condition of Eamzade Hashem tunnel in Iran. *Arab J Geosci* 6:1241–1248
- Song H, Zhang H, Kang Y, Huang G, Fu D, Qu C (2013) Damage evolution study of sandstone by cyclic uniaxial test and digital image correlation. *Tectonophysics* 608:1343–1348
- Tarasov B, Potvin Y (2013) Universal criteria for rock brittleness estimation under triaxial compression. *Int J Rock Mech Min Sci* 59:57–69
- Tarasov BG, Stacey TR (2017) Features of the energy balance and fragmentation mechanisms at spontaneous failure of class I and class II rocks. *Rock Mech Rock Eng* 50:2563–2584
- Townend E, Thompson BD, Benson PM, Meredith PG, Baud P, Young RP (2008) Imaging compaction band propagation in Diemelstadt sandstone using acoustic emission locations. *Geophys Res Lett* 35:L15301
- Tsai LS, Hsieh YM, Weng MC, Huang TH, Jeng FS (2008) Time-dependent deformation behaviors of weak sandstones. *Int J Rock Mech Min Sci* 45:144–154
- Tsang CF, Bernier F, Davies C (2005) Geohydromechanical processes in the Excavation Damaged Zone in crystalline rock, rock salt, and indurated and plastic clays—in the context of radioactive waste disposal. *Int J Rock Mech Min Sci* 42:109–125
- Weng MC, Jeng FS, Huang TH, Lin ML (2005) Characterizing the deformation behavior of Tertiary sandstones. *Int J Rock Mech Min Sci* 42:388–401
- Wong T-f, Baud P (2012) The brittle-ductile transition in porous rock: a review. *J Struct Geol* 44:25–53
- Xu W-y, Nie W-p, Zhou X-q, Shi C, Wang W, Feng S-r (2011) Long-term stability analysis of large-scale underground plant of Xiangjiaba hydro-power station. *J Cent South Univ Technol* 2011:511–520
- Yang S-Q, Jing H-W, Wang S-Y (2012) Experimental investigation on the strength, deformability, failure behavior and acoustic emission locations of red sandstone under triaxial compression. *Rock Mech Rock Eng* 45:583–606
- Yang S-Q, Yang Z, Jing H-W, Xu T (2020) Fracture evolution mechanism of hollow sandstone under conventional triaxial compression by X-ray micro-CT observations and three-dimensional numerical simulations. *Int J Solids Struct* 190:156–180
- Yin P-F, Yang S-Q (2018) Experimental investigation of the strength and failure behavior of layered sandstone under uniaxial compression and Brazilian testing. *Acta Geophys* 66:585–605
- Zhang S, Wu S, Zhang G (2020) Strength and deformability of a low-porosity sandstone under true triaxial compression conditions. *Int J Rock Mech Min Sci* 127:104204

Publisher's Note Springer Nature remains neutral with regard to jurisdictional claims in published maps and institutional affiliations.